iScience

CellPress
OPEN ACCESS

Article

Endothelial tissue remodeling induced by intraluminal pressure enhances paracellular solute transport

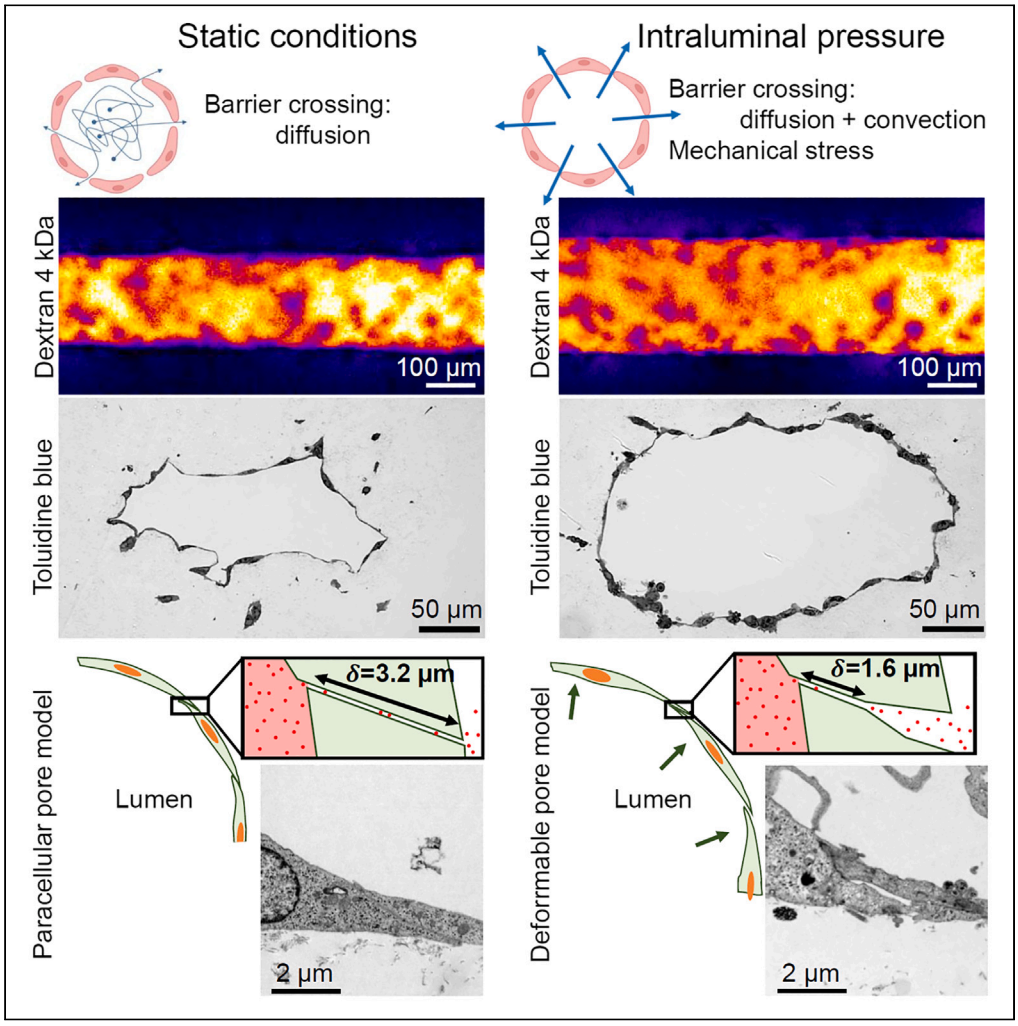

Jean Cacheux, Aurélien Bancaud, Daniel Alcaide, Jun-Ichi Suehiro, Yoshihiro Akimoto, Hiroyuki Sakurai, Yukiko T. Matsunaga

abancaud@laas.fr (A.B.)
mat@iis.u-tokyo.ac.jp (Y.T.M.)

Highlights

Intraluminal pressure enhances the rate of transport across *in vitro* endothelia

Endothelial tissues are strained and remodeled by intraluminal pressure

Data are accounted for by the deformation of paracellular pores through gap thinning

Cacheux et al., iScience *26*, 107141
July 21, 2023
https://doi.org/10.1016/j.isci.2023.107141

iScience

CellPress
OPEN ACCESS

Article

Endothelial tissue remodeling induced by intraluminal pressure enhances paracellular solute transport

Jean Cacheux,[1,2,6] Aurélien Bancaud,[1,2,3,6,7,*] Daniel Alcaide,[1] Jun-Ichi Suehiro,[4] Yoshihiro Akimoto,[5] Hiroyuki Sakurai,[4] and Yukiko T. Matsunaga[1,2,*]

SUMMARY

The endothelial layers of the microvasculature regulate the transport of solutes to the surrounding tissues. It remains unclear how this barrier function is affected by blood flow-induced intraluminal pressure. Using a 3D microvessel model, we compare the transport of macromolecules through endothelial tissues at mechanical rest or with intraluminal pressure, and correlate these data with electron microscopy of endothelial junctions. On application of an intraluminal pressure of 100 Pa, we demonstrate that the flow through the tissue increases by 2.35 times. This increase is associated with a 25% expansion of microvessel diameter, which leads to tissue remodeling and thinning of the paracellular junctions. We recapitulate these data with the deformable monopore model, in which the increase in paracellular transport is explained by the augmentation of the diffusion rate across thinned junctions under mechanical stress. We therefore suggest that the deformation of microvasculatures contributes to regulate their barrier function.

INTRODUCTION

Endothelial layers constitute physical barriers that act as gateways between the blood and the surrounding tissues.[1,2] They mediate exchanges of molecules, such as water, oxygen or proteins, and hence contribute to tissue homeostasis. Dysregulation of the barrier function contributes to the pathophysiology of many diseases, including cancer and infections. Endothelial tissues also constitute physical barriers that have to be crossed for efficient delivery of therapeutic agents.[3] The passage of solutes across these barriers occurs via two non-mutually exclusive mechanisms of transcellular and paracellular transport.[4] The transcellular route crosses apical and basal cell membranes and is mostly mediated by transcytosis, an energy-dependent trafficking of vesicles across the endothelium,[5] or the dynamic formation of patent openings.[6] In contrast, the paracellular pathway, which passes through intercellular spaces between contacting cells,[7] is considered to be passive. It is maintained by the interendothelial junctions, which are mediated by tight junction proteins and adherens junction proteins,[8,9] and/or by rearrangement of their architecture. Although the relative strength and size selectivity of paracellular versus transcellular pathways is tissue-specific and remains the subject of intense research *in vivo*,[10–12] it is considered that, except for cerebral capillaries in which tight junctions are most abundant,[13] small hydrophilic molecules transit through the paracellular route in other microvasculatures.[14–16]

In 2D cell culture systems, the paracellular transport pathway is most frequently characterized by *trans*-endothelial electrical resistance (TEER).[17–19] This technique, which consists in recording the ionic current across a cell tissue on application of an electric field, provides a readout that correlates with the structural integrity of endothelial barriers. Paracellular transport can also be assayed by the leakage or macromolecular assay (MA), which consists in tracking the temporal[20–23] or spatial[24,25] redistribution of fluorescently labeled hydrophilic dextran through the tissue.[26] The readout of the MA is most frequently the diffusive permeability, which can be used to model the intercellular spaces as pores of characteristic diameter ~5 nm for mesenteric capillaries.[7] This estimate is however obtained in the absence of intraluminal pressure, and the consequences of this constitutive cue of the vascular system on transport across the endothelium remain unclear.[27] The pressure gradient across the barrier is indeed expected to create a flow in the

[1]Institute of Industrial Science, The University of Tokyo, Tokyo 153-8505, Japan

[2]LIMMS, CNRS-IIS UMI 2820, The University of Tokyo, Tokyo 153-8505, Japan

[3]CNRS, LAAS, 7 Avenue Du Colonel Roche, 31400 Toulouse, France

[4]Department of Pharmacology and Toxicology, Kyorin University School of Medicine, 6-20-2, Shinkawa, Mitaka, Tokyo 181-8611, Japan

[5]Department of Anatomy, Kyorin University School of Medicine, Mitaka, Tokyo 181-8611, Japan

[6]These authors contributed equally

[7]Lead contact

*Correspondence: abancaud@laas.fr (A.B.), mat@iis.u-tokyo.ac.jp (Y.T.M.)

https://doi.org/10.1016/j.isci.2023.107141

intercellular gaps, and in turn to enhance the apical to basal flux. However, whether diffusion or convection is the dominant transport mechanism in the paracellular pathway is debated in the literature.[28]

In this study, we set up a tissue-engineering approach to compare the strength of paracellular transport in endothelial tissues with or without intraluminal pressure. We use Human Umbilical Vein Endothelial Cells (HUVECs), which represent a standard for *in vitro* studies of vasculature and angiogenesis[29] with an endothelial phenotypic response to mechanical stimulation.[30,31] Using the transport at mechanical rest as a reference, we prove that intraluminal pressure enhances paracellular flux by 135%, strains the tissue by 25%, induces reorganization of the cytoskeleton associated actin stress fiber formation, and remodels the tissue though the formation of clusters of endothelial cells. Electron microscopic observation of intercellular junctions shows that the thickness of the paracellular junctions decreases by ~ 50% in the stretched regions of the tissue. We show that the conventional monopore model[16] of paracellular transport, in which the deformation of the tissue induced by intraluminal pressure is ignored, fails to account for this data. We thus propose the deformable monopore model (DMM) to integrate the consequences of the morphological change of paracellular junctions under pressure on barrier function properties.

RESULTS

Principle of the static and pressure assays

We fabricated microvessels (MV) in collagen gels of 200 μm in diameter and 6 mm in length (Figures 1A and 1B and STAR Methods) following the protocols described by Matsunaga et al.[32,33] After two days of maturation in static conditions (i.e., without intraluminal pressure), we mounted a 3D printed device on top of the MV chip to adjust the level of liquid in the inlets (Figure 1C), and in turn to monitor the conditions of transport across the endothelial barrier. Specifically, the level of liquid over the two inlets and the collagen matrix was even in the static assay (left panel in Figures 1D and 1E). We thus insured a constant pressure on the basal and apical sides of the tissue, and the passage of fluorescent macromolecules across the barrier was only forced by diffusion. In the pressure assay (right panel in Figures 1D and 1E), we did not fill the central reservoir on top of the collagen gel with liquid to apply an intraluminal pressure of 100 Pa (1 cm of fluid height difference). The fluid height difference then remained constant in the time course of the pressure assay experiments that typically lasted two to 3 min because the permeation flow through the MV barrier was too low to change the volume in the inlet reservoirs.

Models of the static and pressure assays

The static and pressure assays started by the injection of two dextran dyes in the lumen at $t = 0$. Their spatial redistribution was then monitored by confocal microscopy in the equatorial plane of the MV. Assuming an axisymmetric geometry, the dynamics of the concentration $C(r,t)$ of macromolecules in the collagen matrix with r the distance to the center of the lumen and t the time is governed by Fick's second law of diffusion with convection:

$$\frac{\partial C}{\partial t} + \frac{V_0}{r}\frac{\partial C}{\partial r} = \frac{D_0}{r}\frac{\partial}{\partial r}\left(r\frac{\partial C}{\partial r}\right) \qquad \text{(Equation 1)}$$

with D_0 the tracer diffusion coefficient in collagen gels and V_0 the permeation flow velocity across the barrier (V_0 is null in the diffusion assay and D_0 is calibrated as described in Figure S1). The endothelial barrier sets the flux of macromolecules per unit of tube length that leaks out from the lumen to the collagen. In the static assay, this flux $J_D(t)$ is determined by the difference between the apical and basal concentrations C_{in} and C_{out}, respectively, multiplied by the diffusive permeability $\mathcal{L}_D$[16,34]:

$$J_D(t) = 2\pi r_0 \mathcal{L}_D (C_{in}(t) - C_{out}(t)) \qquad \text{(Equation 2)}$$

with r_0 the radius of the tube.

Convective and diffusive solute transport contribute to the flux $J_P(t)$ in the pressure assay. It can be expressed with the Patlak equation[7]:

$$J_P(t) = 2\pi r_0 C_{in} V_0 \left(1 + \frac{1 - \frac{C_{out}}{C_{in}}}{e^{Pe} - 1}\right) \qquad \text{(Equation 3)}$$

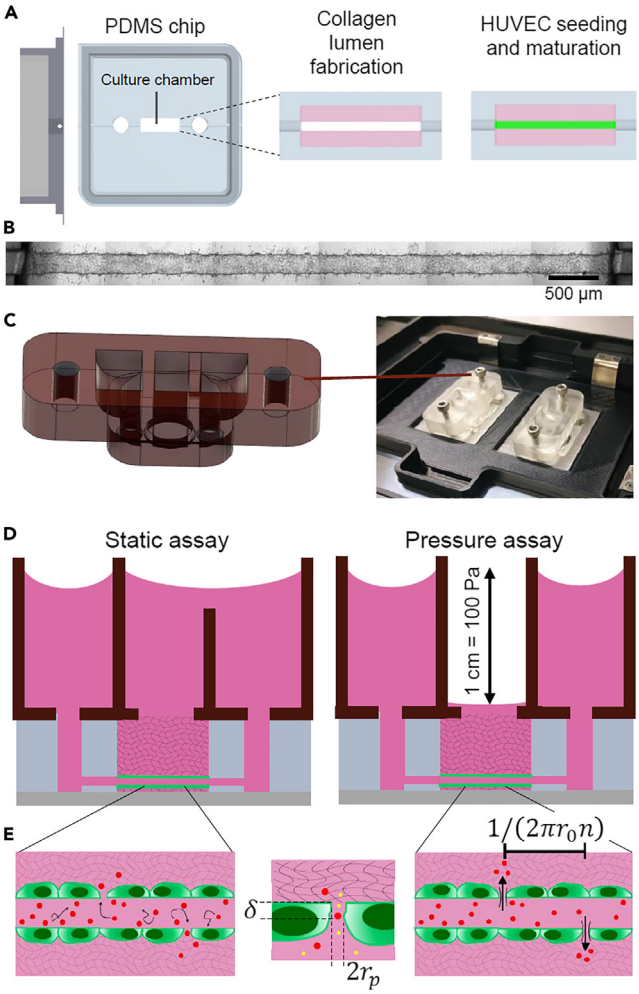

Figure 1. MV fabrication and characterization by the static and pressure assays

(A) Representation of the microvessel chip and the consecutive fabrication steps starting from Human Vascular Endothelial Cells (HUVEC). The chip is represented in gray, the collagen gel in pink, and the endothelial tissue in green.

(B) Microscopic view of an MV after two days of culture. Note that we always detected some outgrowth of endothelial cells in the collagen gel after the maturation. The scale bar corresponds to 500 µm.

(C) Layout of the 3D printed device for the static assay, and photograph of the device in operation on an inverted microscope.

(D) Schematic representation of the devices to run the static and pressure assays. Intraluminal pressure is produced by 1 cm of hydrostatic pressure.

(E) The left and right panels represent the transport of tracers through the barrier using diffusion or pressure as actuation scheme, respectively. The central panel shows the monopore model, as defined by the pore radius r_p, density n, and thickness δ. We investigate the passage of two macromolecules with different sizes across paracellular junctions, as shown with red and yellow circles.

with $Pe = V_0/\mathcal{L}_D$ the Peclet number that represents the ratio of the convection to diffusion rate in the intercellular gaps. On the vanishing Pe limit, Equation 3 is the same as Equation 2. Note that Equation 3 is readily obtained by computing the flux through a single pore,[35] and summing the total flux over all the pores traversing the tissue. In the following, we describe and check the consistency of two methods to infer $\mathcal{L}_D$ and $V_0/\mathcal{L}_D$.

Extraction of $\mathcal{L}_D$ from the static assay

The flux $J_D(t)$ across the barrier in the static assay is equal to the temporal variation of the number of macromolecules $N_{out}(t)$ in the collagen gel. This number $N_{out}(t)$ can readily be extracted from confocal images by computing the integral of the concentration profile $\int_{r_0}^{r_{max}} C(r,t)2\pi r dr$ between the MV basal layer to the

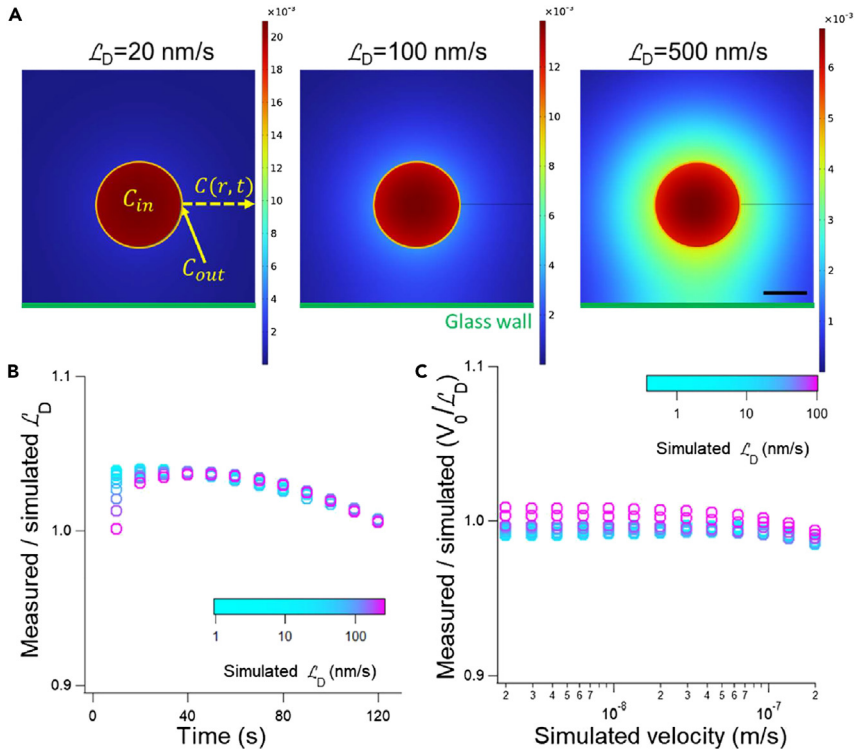

Figure 2. Validation of the static and pressure assays by finite element modeling

(A) The snapshots represent the cross-section of the MV with the lumen shown in red, the cell layer in orange, and the collagen gel in blue. In the static assay, the tissue is modeled by its diffusive permeability $\mathcal{L}_D$, as indicated in the legend, and the simulations represent the concentration fields after a time lag of 200 s (the three heat maps are in units of mol/m^3). We extract the basal and apical concentrations C_{out} and C_{in}, respectively, and the concentration profile $C(r,t)$ along the dashed yellow arrow. The scale bar corresponds to 100 μm.

(B) The plot reports the ratio of the measured to the simulated $\mathcal{L}_D$, as indicated in the color scale, as a function of time.

(C) The plot presents the ratio of the measured $V_0/\mathcal{L}_D$ divided by this input parameter of the simulations as a function of the permeation velocity across the tissue V_0. Data points are color-coded according to the value of the diffusive permeability, as indicated in the color scale.

limit of the field of observation r_{max} (i.e., along the yellow dashed line in Figure 2A). Hence, the diffusive permeability can be expressed from Equation 2:

$$\mathcal{L}_D = \frac{dN_{out}/dt}{2\pi r_0 (C_{in} - C_{out})} \quad \text{(Equation 4)}$$

We validated the accuracy of Equation 4 by running finite element simulations (see STAR Methods) to take the geometrical settings of the experiments into account. We extracted C_{in}, C_{out}, and dN_{out}/dt from the simulations (Figure 2A), determined $\mathcal{L}_D$ using Equation 4 and compared this parameter to the input of the simulations (see legend of Figure 2B). We concluded that this method was accurate because the difference between the measured and the simulated $\mathcal{L}_D$ was less than 3% during the first 200 s of the simulation (Figure 2B). Notably, the smooth decrease of $\mathcal{L}_D$ over time is readily explained by the escape of tracers from the field of observation of the microscope, which biases the determination of the flux $J_D(t)$ because of the error on the integral of $C(r,t)$.

Extraction of $V_0/\mathcal{L}_D$ from the pressure assay

For the analysis of the pressure assay, one should compare the rate of convection and diffusion in the collagen gel, which is gauged by the ratio $V_0 r_0/D_0$. Taking typical values of r_0, V_0, and D_0 of 100 μm, 0.1 μm/s, and 250 μm^2/s (see below), the latter ratio is ~0.05. Hence, the convection rate is negligible compared to the diffusion rate. It implies that the equation governing fluorescence spatial redistribution

in the pressure assay is the same as in the static assay, but the flux of molecules crossing the barrier $J_P(t)$ is different. By computing the ratio $J_P(t)/J_D(t)$, we obtain an expression of $V_0/\mathcal{L}_D$:

$$\frac{J_P(t)}{J_D(t)} = \frac{\partial C_P/\partial r(r,t)}{\partial C_D/\partial r(r,t)} = \frac{C_P(r,t)}{C_D(r,t)} = \frac{1}{\left(1 - \frac{C_{D\,out}}{C_{in}}\right)} \frac{V_0}{\mathcal{L}_D} \left[1 + \frac{1 - \frac{C_{P\,out}}{C_{in}}}{e^{\frac{V_0}{\mathcal{L}_D}} - 1}\right] \quad \text{(Equation 5)}$$

with $C_{D\,out}$ and $C_{P\,out}$ the basal concentrations in the static and pressure assays, respectively. Consequently, $V_0/\mathcal{L}_D$ can be inferred from the numerical inversion of Equation 5 knowing the concentration profile measured with the pressure and static assay.

We validated this method using finite element simulations in which the permeation velocity V_0 and the diffusive permeability $\mathcal{L}_D$ varied in the range of 1–200 nm/s. For each simulation, we extracted the concentration profile for the pressure assay after 30 s and normalized it with the output of simulations of the static assay to measure $V_0/\mathcal{L}_D$ using Equation 5. We computed the ratio of the resulting value of $V_0/\mathcal{L}_D$ divided by the input of the simulations, and plotted this parameter in Figure 2C. This graph showed that the measured value of $V_0/\mathcal{L}_D$ was consistent with that of the simulation, and the error was lower than 5% for a broad range of experimental conditions.

The static assay predicts a size of paracellular pores of 24 nm

The integrity of endothelial tissues correlates the permeation properties of the barrier, but it remains unclear if the structure of paracellular pores can be inferred from permeation measurements on MVs. We thus started by performing the static assay using MVs after two days of maturation. Note that the maturation of the tissue occurred without any intraluminal pressure (*i.e.*, in the same conditions as the static assay). We used nine MVs and nine fixed MVs, which were characterized by an average radius r_0 of 102 $\pm$ 2 μm (see Figure S2 for edge detection strategy) that was comparable to the radius of the lumen before cell seeding of 100 μm. The static assay was operated by simultaneously injecting two dextran probes of 4 and 70 kDa labeled with spectrally separated dyes in the lumen of MVs. The spatial redistribution of these macromolecules was then monitored by confocal microscopy for ~200 s (Figure 3A and Methods) using a square field of observation of 1.3 mm that represented a fraction of ~20% of the MV total length of 6 mm. Given that the thickness of confocal stacks was 12 μm, we probed the diffusion across a tissue surface of ~30,000 μm^2. Using confocal immunofluorescence micrographs of MV labeled with the junction protein vascular endothelial cadherin (VE-Cad) and DNA (Figure 3C), we counted ~100 $\pm$ 11 cells over a comparable surface, implying that our measurements correspond the diffusive transport properties averaged over ~100 paracellular junctions.

To estimate the diffusive permeability based on Equation 4, we then measured the intraluminal and basal concentrations C_{in} and C_{out} (green and orange rectangles in Figure 3A, respectively), and the number of tracers N_{out} in the collagen matrix from the spatial integration of the intensity profile in the red dashed area in Figure 3A. We detected opposite trends for the variation of C_{in} and C_{out} in 200 s characterized by a decrease of 20% and an increase of 19%, respectively (green and orange datasets). This observation was readily explained by the escape by diffusion of dextran molecules from the lumen to the collagen gel. The amplitude of the concentration gradient across the barrier, which is proportional to $(C_{in} - C_{out})$ (see Equation 2), thus decreased in time, leading to a reduction of the rate of barrier crossing in the course of the experiment. This assumption was confirmed by monitoring the variation of N_{out} over time (red dashed curve reported in the right y axis of Figure 3C), because this readout increased more rapidly at the beginning of the experiment than after 200 s (black solid line as guide to the eye in Figure 3C). We finally used the three readouts to extract the diffusive permeability for the 4 and 70 kDa dextran (Figure 3D). In contrast to C_{in}, C_{out}, and N_{out} which were unsteady variables in time, the diffusive permeability appeared to be constant in time, as expected for an intrinsic parameter of the endothelial barrier. We finally computed the temporal average of the diffusive permeability of 91.3 $\pm$ 8.5 and 10.9 $\pm$ 2.2 nm/s for the 4 and 70 kDa dextran, respectively (purple and orange datasets in Figure 3C).

This operation was repeated on the nine MV samples to estimate the average diffusive permeability $\mathcal{L}_D$ of 87 $\pm$ 13 nm/s for the 4 kDa dextran, which was comparable to the estimate in *in vitro* systems,[36] but was slightly higher than the value reported for skeletal muscle microvasculatures of 10 nm/s.[37] $\mathcal{L}_D$ was 14 $\pm$ 3 nm/s for the 70 kDa dextran (*i.e.*, 6.2 times lower than for the 4 kDa dextran). We performed the same

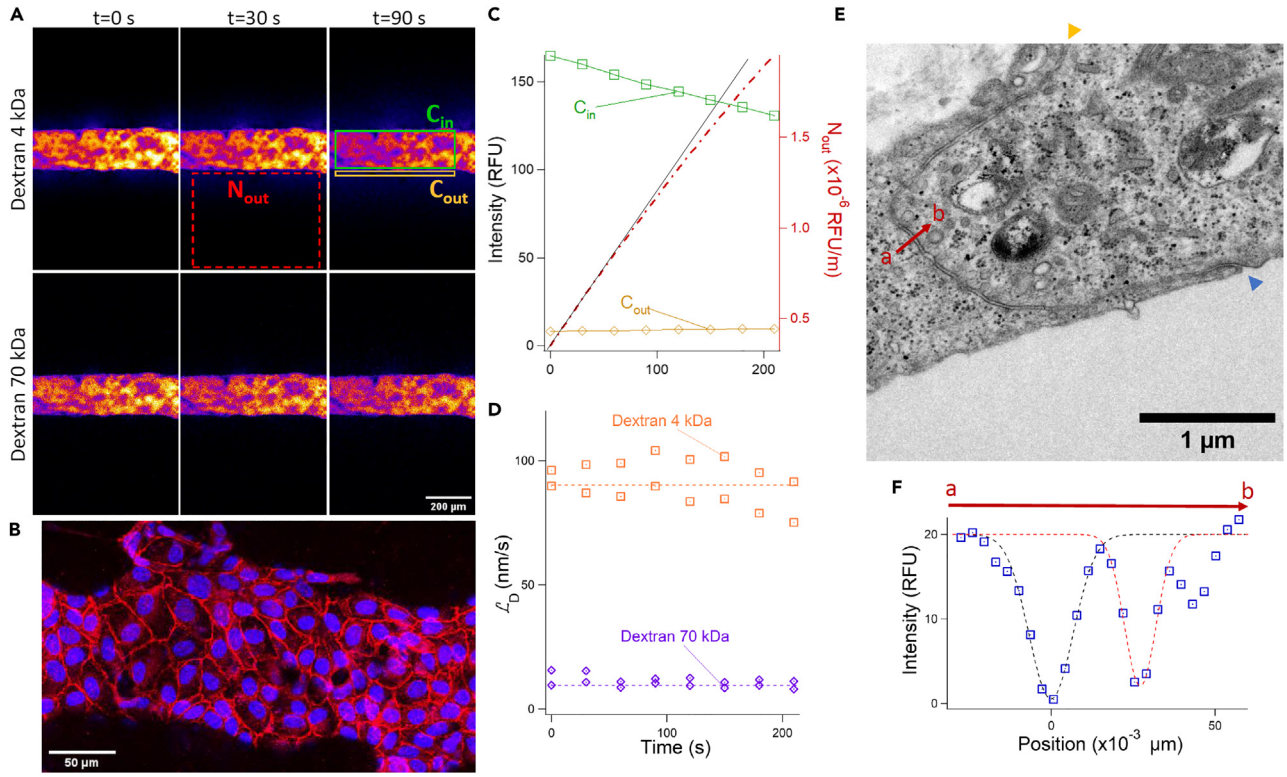

Figure 3. MV characterized by the static assay

(A) The two confocal time series represent fluorescence spatial redistribution for the 4 and 70 kDa dextran. The number of molecules N_{out} that crossed the barrier is measured at each time step in the collagen matrix (red rectangle). The intraluminal and basal concentrations C_{in} and C_{out} are inferred from the maximum and mean intensity in the green and yellow rectangles, respectively. The scale bar corresponds to 200 µm.

(B) Maximum intensity projection of confocal micrographs of the junctions between the endothelial cells of MVs cultured in static conditions. Junctions are visualized by immunofluorescence detection of vascular endothelial cadherin (VE-Cad) and nuclei with Hoechst 33342. The scale bar corresponds to 50 µm.

(C) The graph shows the temporal variation of C_{in} and C_{out} on the left axis for the 4 kDa dextran and $N_{out}(t)$ on the right axis with the color code of panel A.

(D) The plot presents the diffusive permeability for the 4 and 70 kDa dextran as a function of time. At each time point, we measure two times the diffusive permeability using each side of the MV. Dashed lines correspond to temporal averages.

(E) Transmission electron micrograph of one endothelial cell junction. The blue and orange arrowheads indicate the apical and basal sides of the gap, respectively. The scale bar corresponds to 1 µm.

(F) The plot shows the spatial variation of the signal along the red arrow in (E). Dashed lines are Gaussian fits to measure the size of the paracellular gap.

characterization with the nine fixed samples, and obtained very comparable values for the diffusive permeability of 107 ± 20 nm/s and 14 ± 3 nm/s for the 4 kDa and 70 kDa dextran, respectively, implying that we could not detect any degradation of the tissue integrity associated with the fixation process.

We finally used the diffusive permeability to assess the structure of paracellular pores. The variation of the diffusive permeability of the 4 versus 70 kDa dextran is 6.2-fold, whereas the change in diffusion coefficient between these macromolecules is 3.9-fold (see characterization in Figure S1). This difference is explained by the confinement of the tracers in the intercellular gaps (see the scheme with red and yellow probes in Figure 1D). Confinement is indeed known to enhance the friction and slow down the diffusion of probes across pores (see Equation 7 in the STAR Methods section), and this consequence increases as the size of the tracer r_{dye} becomes comparable to that of the pore r_p.[35] Using a mathematical function to model this effect, a common approximation in the field,[16,35] we can use the variation of the diffusive permeability to fit the level of confinement r_{dye}/r_p, and in turn to infer the size of paracellular pores. This approach can be performed on the nine MVs independently to obtain an average pore size r_p of 24 ± 3 nm (note that the fitted pore size is the same for fixed MVs). The analysis is strongly supported by transmission electron microscopic observation of MV thin sections (Figure 3E and STAR Methods), which show that the pore radius is on the same order of magnitude of 13 ± 2 nm (Figure 3F, average over four micrographs of junctions). Consequently, the structure of paracellular gaps inferred from functional diffusion-based

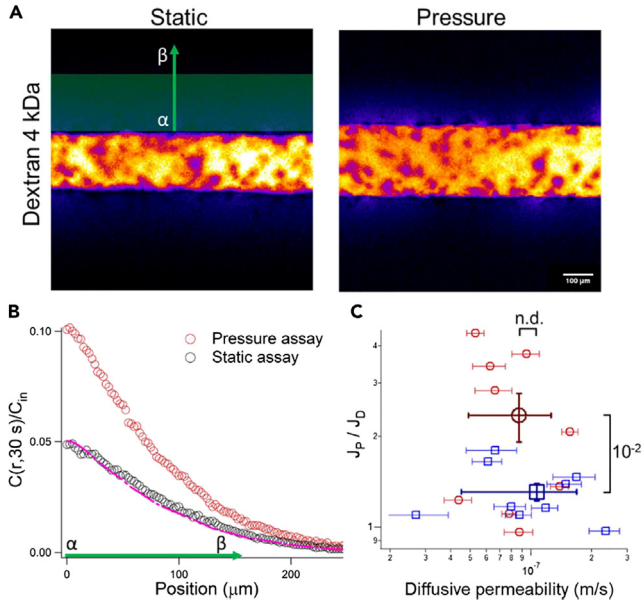

Figure 4. MV characterized by the pressure assay

(A) Fluorescence confocal micrographs of the same MV recorded 30 s after the injection of dextran using the static and pressure assays. The scale bar corresponds to 100 µm.

(B) The red and black datasets represent the concentration profile as obtained from the pressure and static assay, respectively. The profiles are recorded along the green axis in (A) between the marks α and β. The pink dashed line is response of the pressure assay after normalization of its maximum to that of the static assay.

(C) Ratio of the flux across the MV barrier in the pressure to static assay as a function of the diffusive permeability $\mathcal{L}_D$ for live and fixed samples (red and blue datasets, respectively). Data is expressed as average ±standard error. The averages values are marked with large symbols for both conditions, and unpaired Student's *t* test is used for statistical analysis (shown with brackets).

measurements are corroborated by electron microscopic inspection, implying that transport data provide a direct readout of the integrity of endothelial tissues.

The pressure assay predicts a size of paracellular pores of 179 nm

Whether the structure of paracellular pores is altered by intraluminal pressure remains unclear. Hence, we performed the pressure assay on the same MV samples to obtain a quantitative comparison of the paracellular flux with or without stress on the tissue. We set the intraluminal pressure to 100 Pa to apply a static mechanical stress, the amplitude of which was comparable to the pulsatile pressure in human capillaries of ~500 Pa.[38] We then injected the 4 kDa dextran in the lumen (Figure 4A), and extracted the concentration profile after a time lag of 30 s (see model section and red dataset in Figure 4B). This time interval was selected to obtain a sharp concentration profile easily comparable to the outcome of the static assay (black dataset in Figure 4B). The greater amplitude of the concentration profile in the pressure assay indicated that intraluminal pressure increased the transport rate across the barrier. As hypothesis-free readout of these experiments, we computed the flux of fluorescent tracers crossing the barrier $J_P(t)$ in the pressure assay and normalized it with that of the static assay J_P/J_D. This measurement indeed allowed us to determine to what extent pressure actuation increased the transport of tracers across the barrier. We averaged J_P/J_D over the nine samples, and deduced that 2.35 ± 0.43 times more molecules were transported across the MV with intraluminal pressure (red dataset in Figure 4C). In the fixed samples, this ratio was comparatively lower and equal to 1.35 ± 0.10 (blue dataset in Figure 4C).

On normalization of the concentration profiles in the pressure and static assays, the responses were superposed (pink dashed lines versus black datasets in Figure 4B). This response readily showed that fluorescence redistribution in collagen gels was dominated by diffusion even with intraluminal pressure, as explained in the model section. This statement was further borne out on characterizing one leaky barrier, which was obtained by loading a low number of cells in the duct. Indeed, the concentration profile in

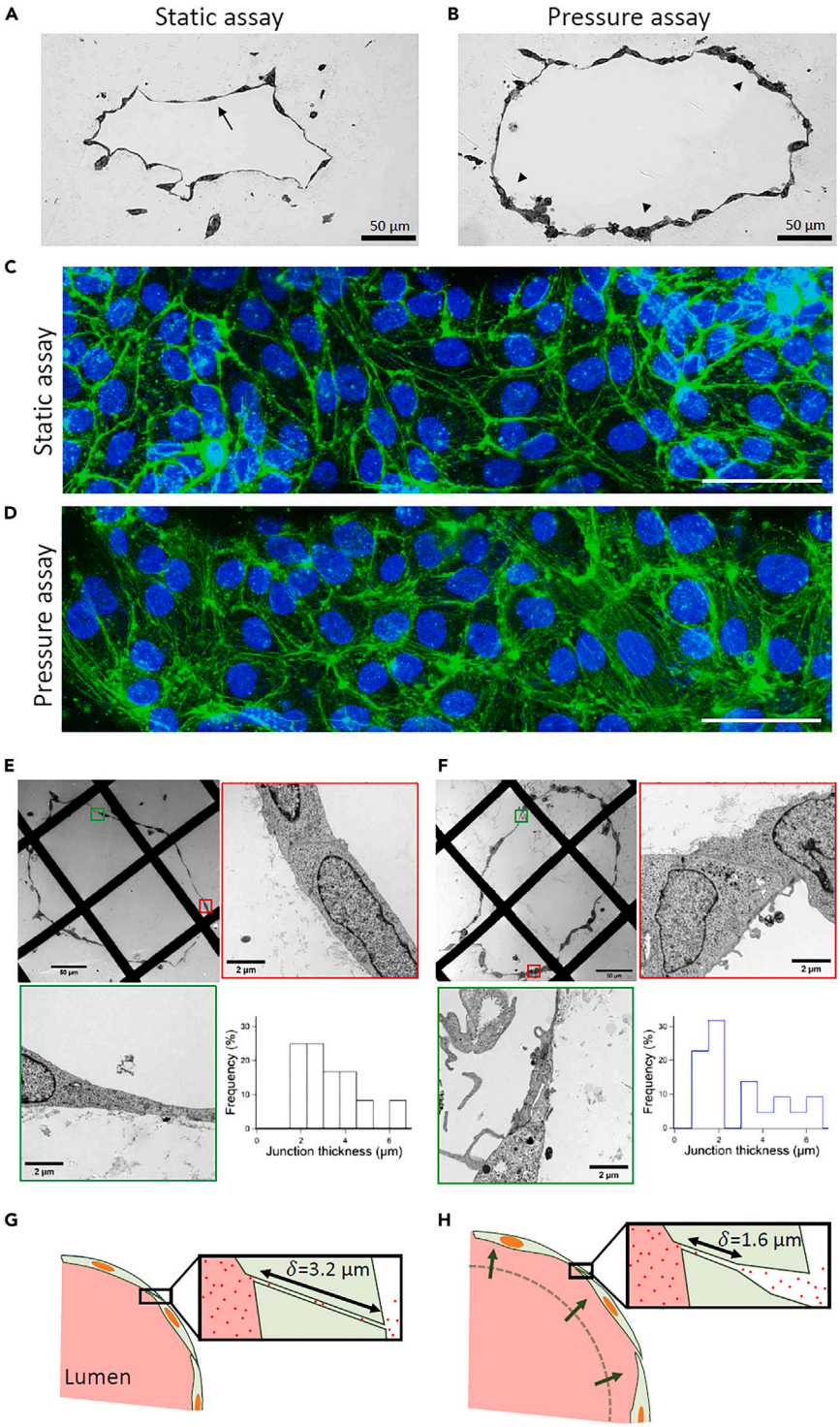

Figure 5. Structure of MVs in the static and pressure assay

The results of the static assay are shown in the panels (A, C, E), and those of the pressure assay in (B, D, F).

(A and B) Optical micrographs of MV sections stained with toluidine blue. The arrow in (A) shows the lining of endothelial cells, and the arrowheads in (B) the clusters of endothelial cells. The scale bars correspond to 50 µm.

(C and D) Maximum intensity projection of confocal micrographs obtained by staining MV with phalloidin for the detection of fibril actin in green and nuclear DNA in blue. The MV were fixed just after the static and pressure assays. The scale bars correspond to 50 µm.

Figure 5. *Continued*
(E and F) Transmission electron micrographs of MVs at different levels of magnification. The red and green outlines correspond to the zooms of the squares in the low magnification image. The histograms show the distribution of paracellular junction thickness with 12 counts in (E) and 22 in (F). The scale bars correspond to 2 μm.
(G and H) Representation of the deformable monopore model to account for the data from the static and pressure assays.

the pressure assay did not match that of the static assay (Figure S3). Furthermore, structural inspection of thin MV sections by transmission microscopy did not show an enhanced frequency of caveolae in the static and pressure assays (Figure S4). Altogether, we could thus use Equation 5 to analyze our datasets. Specifically, the ratio J_P/J_D enabled us to determine the ratio $V_0/\mathcal{L}_D$ of the permeation flow velocity to the diffusive permeability, which was equal to 1.91 $\pm$ 0.54. We then considered the predictions of the pore model to determine the paracellular pore size from these measurements (see Equation 9 in the STAR Methods section; note that the size of the 4 kDa dextran of 1.5 nm is smaller than the pore size, implying that the hindrance factor is equal to 1 in Equation 9). We deduced that the average paracellular pore size r_p of 179 nm was 7.5-fold wider than the dimension inferred from the static assay of 24 nm. The integrity of MVs hence appeared to be altered on application of intraluminal pressure, prompting us to investigate the structure of paracellular junctions by transmission electron microscopy.

Structural analysis of MVs in the pressure and static assays

Starting from macroscopic observations, we noted that the radius of MVs increased by 25 $\pm$ 1% from 102 $\pm$ 2 to 128 $\pm$ 2 μm on application of intraluminal pressure (Figures 4A and S5). Immediately after the pressure and static assays, MVs were fixed, sliced in thin sections, and characterized by optical microscopy using toluidine blue staining[39] (Figures 5A and 5B). The samples from the static assay had a conventional phenotype of endothelial tissues with an even distribution of elongated cells and flat nuclei over the contour of the vessel (arrows in Figure 5A). The application of intraluminal pressure induced a drastic morphological change associated with the formation of clusters of cells (arrowheads in Figure 5B). These clusters represented a fraction of the contour of the tissue of 35.4% that was 4.4 times larger than that in the static assay of 8.1%, as inferred from the analysis of four micrographs for each condition. Consequently, the application of intraluminal pressure reorganized the tissue. Bearing in mind that the strain of 25% activates endothelial remodeling in cyclic stretch experiments on 2D cultures,[40,41] we focused on the architecture of the actin cytoskeleton with immunostaining (Figures 5C and 5D). We detected predominant cortical actin rings patterns at rest with the presence of occasional stress fibers in the cells (red arrows). On the contrary, transcellular actin stress fibers was the most frequent pattern on application of intraluminal pressure. Given that actin mediates the movement of nuclei within the cell,[42] we suggest that the formation of stress fibers, which is associated with tensile forces,[43] accounts for the clustering of cell nuclei. Despite the remodeling of the tissue, the patterns of VE-Cad, which has a key role in the maintenance of vascular integrity,[2] appeared to be broader but without gaps on mechanical stimulation (Figure S6). Notably, this observation was not comparable to the readout of cyclic stretch experiments, which showed the partial disassembly of adherens junctions associated with barrier function weakening for a strain of 18%.[40]

We finally aimed at clarifying whether the structure of the paracellular junctions was altered by the mechanical stress using high magnification transverse electron microscopy. At mechanical rest, we noted two different patterns of junctions (Figure 5E). In contacting cells with close nuclei, the paracellular cleft across the endothelium was mainly aligned along the apical-to-basal axis, and the thickness of the junction was commensurate with that of the nuclei on the order of 3–5 μm (micrograph with the red contour in Figure 5E). In the thin regions of the tissue, most junctions were tilted with respected to the basal to apical direction, insuring a long cleft of 3–4 μm between contacting cells (micrograph with the green contour in Figure 5E). Hence, despite the observation of two different junction morphologies in the static assay, the distribution of the thickness of paracellular junctions at rest was relatively homogeneous in the range of 2–5 μm with an average of 3.20 $\pm$ 0.35 μm (histogram in Figure 5E). In the pressure assay, a similar classification could be proposed in between the clusters of cells and the thin regions of the tissue. In the cell clusters, we noted that the change in cellular morphology was associated with the reorganization of nuclei, which were no longer elongated along the collagen gel scaffold (*e.g.*, compare the panels outlined in red in Figures 5E and 5F). The paracellular junctions, which remained aligned with the basal to apical direction (micrograph with the red contour in Figure 5F), thickened in the range of 4–6 μm with an average of 5.3 μm. Conversely, in the thin regions of the tissue (micrograph with a green contour in Figure 5F), paracellular junctions appeared to thin down with an average thickness of 1.6 μm. The resulting distribution of junction thickness in Figure 5F was bimodal because of these marked morphological differences. Focusing on the radius of the

Table 1. Overview on MV properties obtained from the DMM for an intraluminal pressure of 100 Pa

Pore size r_p (nm)	Paracellular barrier thickness δ (μm)	Pore density n (μm^{-2})	Porosity φ (%)	Permeability κ (10^{-19} m^2)
24 ± 3	3.2 ± 0.4	0.85 ± 0.31	0.16 ± 0.05	1.2 ± 0.6

paracellular junctions, we did not detect the wide openings of 179 nm that were predicted by the analysis of the flux in the static versus pressure assays. Our data rather hinted to the thinning of the barrier cleft as a consequence of intraluminal pressure, which we aimed to integrate in a model of paracellular transport.

Data integration with the deformable monopore model (DMM)

We describe the DMM to recapitulate our paracellular transport data recorded in the static and pressure assay. This model assumes that (i) the pore radius is constant and equal to 24 nm in both assays (Figures 5G and 5H) and (ii) the paracellular junction thickness is reduced under intraluminal pressure (Figure 5H). The latter hypothesis implies that the diffusive permeability, which is inversely proportional to the barrier thickness according to Equation 7 in the STAR Methods section, increases in the pressure assay in comparison to the static assay (denoted $\mathcal{L}_{DP}$ in Equation 10). This consequence of the deformation of the tissue changes the ratio of the diffusive to convective flux across the barrier J_P/J_D, as reformulated in Equation 10. The permeation velocity to the diffusive permeability $V_0/\mathcal{L}_D$ is only dependent on the paracellular pore radius (see Equation 9), allowing us to determine its value of 7.3×10^{-3} for an intraluminal pressure of 100 Pa. Knowing that J_P/J_D is 2.35 ± 0.43, we then fit the ratio of the diffusive permeability in the pressure to static assay $\mathcal{L}_{DP}/\mathcal{L}_D$ of 1.9 ± 0.3. The DMM hence indicates that the junction thickness is divided by 1.9 on application of intraluminal pressure. This value is in agreement with electron microscopic data, which shows a reduction of the pore thickness by a factor of ~2 from 3.2 to 1.6 μm in the thin regions of the tissue. We note that the DMM predicts that the ratio $V_0/\mathcal{L}_{DP}$ of the permeation velocity to the diffusive permeability in the pressure assay is lower than 10^{-2}. Paracellular transport is thus dominated by diffusion even with intraluminal pressure, and the onset of cross-barrier flux is explained by the thinning of paracellular junctions, which is associated with an onset in diffusive permeability. Of interest, this suggestion is borne out by the fact that the augmentation of flux across the barrier J_P/J_D is reduced from 2.35 to 0.35 in live versus fixed samples. The fixation process indeed reduces MV deformation from 25 to 5% (Figure S5), and impedes the remodeling of the tissue under intraluminal pressure that is associated with the onset in diffusive permeability.

DISCUSSION

We provide technologies and analytical methods to characterize molecular transport across endothelial layers in 3D microvessel structures. We prove that intraluminal pressure increases cross-barrier flux, and explain it with the DMM, which speculates that the diffusive permeability increases under pressure as a consequence of the remodeling of the endothelial tissue and the thinning of paracellular junctions. Using this model, we can specify the structural and functional properties of MV barriers (Table 1). Given the pore size r_p and cleft thickness δ from the static assay, we deduce the pore density from Equation 7 of ~1 pore/μm^2. This estimate is in excellent agreement with the measurements in mesenteric capillaries.[7] The resulting porosity, which represents the surface fraction of pores over the MV contour, is 0.2%, showing that endothelial barriers offer little room to the passage of diffusing tracers. The permeation properties of the tissue can also be derived from Equation 8, yielding κ of 10^{-19} m^2. This value, which compares to that of impermeable shale sedimentary rocks,[44] shows that MV constitute impermeable tissues, which nevertheless enable the passage by diffusion of molecules of ~10 nm, a size range that matches that of most plasma proteins.[45] Note that the permeability is obtained for an intraluminal pressure of 100 Pa, and we anticipate this parameter to show a complex non-linear response as a function of the pressure settings, a project as yet to be studied. Finally, we suggest that paracellular transport across endothelial tissues can be controlled by their deformation without any change in adherens junction protein expression. It is thus tentative to speculate that the stiffening of the supporting matrix, which is an age-related phenotype,[46] can restrict the deformation of the barrier, reduce exchange through the endothelium, and contribute to unbalanced homeostasis in aged tissues.

It should nevertheless be noted that the MV platform is significantly different from the capillary vasculatures *in vivo*, which are much smaller in diameter (around 10 μm in diameter). Small vessels with a diameter of

200 μm contain a basement membrane and may contain one or multiple layers of smooth muscle cells. Although we noted that HUVECs create a dense basal layer of collagen in MVs (Figure S7), it remains to be clarified how these geometrical, chemical and biological components will influence the transport of components through the vessel wall, but also contribute to a dynamic regulation of the vessel properties. The challenge of integrating more physiological cues in the MV platform and associate them with the unique potential for quantitative measurements will likely be rewarded with an enhanced understanding of the function of the vascular system.

Limitations of the study

Although our study provides generic methods to characterize the permeation properties of microvessels, it suffers from the inherent limitations of *in vitro* systems of the vascular system, as partly enumerated in the conclusion. The diameter of microvessels is much larger than that of capillary vasculatures, the matrix surrounding microvessels is only composed of type I collagen at a low concentration, HUVEC cells have only be loaded in the microvessel, smooth muscle cells/pericytes have not been integrated in the collagen gel, and we do not apply fluid shear stress on microvessels.

STAR★METHODS

Detailed methods are provided in the online version of this paper and include the following:

- KEY RESOURCES TABLE
- RESOURCE AVAILABILITY
  - Lead contact
  - Materials availability
  - Data and code availability
- EXPERIMENTAL MODEL AND STUDY PARTICIPANT DETAILS
- METHOD DETAILS
  - MV fabrication
  - Fixation, immunostaining and electron microscopy
  - Setting up the static and pressure assays
- QUANTIFICATION AND STATISTICAL ANALYSIS
  - Image analysis and statistical analysis
  - COMSOL simulations
  - Expression of L_D and V_0 as a function of the pore geometry
  - Deformable monopore model

SUPPLEMENTAL INFORMATION

Supplemental information can be found online at https://doi.org/10.1016/j.isci.2023.107141.

ACKNOWLEDGMENTS

JC acknowledges the JSPS for postdoctoral fellowship. DA acknowledges the WINGS-QSTEP program for doctoral fellowship. This research was partly supported by the Grant-in-Aid for JSPS Fellows (20F20806), AMED P-CREATE (JP18cm0106239h0001), JSPS Core-to-Core Program (JPJSCCA20190006), AMED-CREST (22gm1510009). The authors thank the LIMMS (CNRS-Institute of Industrial Science, University of Tokyo) for financial support, and Eri Otsuka, Tadaaki Nakajima, and Takanori Sano for technical assistance and critical reading of the manuscript. The authors also thank Sachie Matsubara (Laboratory for Electron Microscopy, Kyorin University School of Medicine) for technical assistance with electron macroscopy.

AUTHOR CONTRIBUTIONS

J.C., A.B., and Y.T.M. conceived and supervised the project; J.C., A.B., and D.A. performed the experiments; J.C. and A.B. developed the models and analyzed the data; J.I.S., Y.A., and H.S. supervised electron microscopy experiments; J.C. and A.B. wrote the original draft; J.C., A.B., D.A., J.I.S., Y.A., H.S., and Y.T.M. contributed to writing – review and editing.

DECLARATION OF INTERESTS

The authors declare no competing interest.

Received: February 23, 2023
Revised: April 27, 2023
Accepted: June 12, 2023
Published: June 15, 2023

REFERENCES

1. Mullin, J.M., Agostino, N., Rendonhuerta, E., and Thornton, J.J. (2005). Keynote review: Epithelial and endothelial barriers in human disease. Drug Discov. Today *10*, 395–408. https://doi.org/10.1016/S1359-6446(05)03379-9.

2. Bazzoni, G., and Dejana, E. (2004). Endothelial Cell-to-Cell Junctions: Molecular Organization and Role in Vascular Homeostasis. Physiol. Rev. *84*, 869–901. https://doi.org/10.1152/physrev.00035.2003.

3. Gładysz, M.Z., Stevanoska, M., Włodarczyk-Biegun, M.K., and Nagelkerke, A. (2022). Breaking through the barrier: Modelling and exploiting the physical microenvironment to enhance drug transport and efficacy. Adv. Drug Deliv. Rev. *184*, 114183. https://doi.org/10.1016/j.addr.2022.114183.

4. Komarova, Y., and Malik, A.B. (2010). Regulation of Endothelial Permeability via Paracellular and Transcellular Transport Pathways. Annu. Rev. Physiol. *72*, 463–493. https://doi.org/10.1146/annurev-physiol-021909-135833.

5. Minshall, R.D., Tiruppathi, C., Vogel, S.M., and Malik, A.B. (2002). Vesicle formation and trafficking in endothelial cells and regulation of endothelial barrier function. Histochem. Cell Biol. *117*, 105–112. https://doi.org/10.1007/s00418-001-0367-x.

6. Fung, K.Y.Y., Fairn, G.D., and Lee, W.L. (2018). Transcellular vesicular transport in epithelial and endothelial cells: Challenges and opportunities. Traffic *19*, 5–18. https://doi.org/10.1111/tra.12533.

7. Rippe, B., and Haraldsson, B. (1994). Transport of macromolecules across microvascular walls: the two-pore theory. Physiol. Rev. *74*, 163–219. https://doi.org/10.1152/physrev.1994.74.1.163.

8. Wallez, Y., and Huber, P. (2008). Endothelial adherens and tight junctions in vascular homeostasis, inflammation and angiogenesis. Biochim. Biophys. Acta *1778*, 794–809. https://doi.org/10.1016/j.bbamem.2007.09.003.

9. Claesson-Welsh, L., Dejana, E., and McDonald, D.M. (2021). Permeability of the Endothelial Barrier: Identifying and Reconciling Controversies. Trends Mol. Med. *27*, 314–331. https://doi.org/10.1016/j.molmed.2020.11.006.

10. Sindhwani, S., Syed, A.M., Ngai, J., Kingston, B.R., Maiorino, L., Rothschild, J., MacMillan, P., Zhang, Y., Rajesh, N.U., Hoang, T., et al. (2020). The entry of nanoparticles into solid tumours. Nat. Mater. *19*, 566–575. https://doi.org/10.1038/s41563-019-0566-2.

11. Kingston, B.R., Lin, Z.P., Ouyang, B., MacMillan, P., Ngai, J., Syed, A.M., Sindhwani, S., and Chan, W.C.W. (2021). Specific Endothelial Cells Govern Nanoparticle Entry into Solid Tumors. ACS Nano *15*, 14080–14094. https://doi.org/10.1021/acsnano.1c04510.

12. Knowland, D., Arac, A., Sekiguchi, K.J., Hsu, M., Lutz, S.E., Perrino, J., Steinberg, G.K., Barres, B.A., Nimmerjahn, A., and Agalliu, D. (2014). Stepwise Recruitment of Transcellular and Paracellular Pathways Underlies Blood-Brain Barrier Breakdown in Stroke. Neuron *82*, 603–617. https://doi.org/10.1016/j.neuron.2014.03.003.

13. Kniesel, U., and Wolburg, H. (2000). Tight junctions of the blood-brain barrier. Cell. Mol. Neurobiol. *20*, 57–76. https://doi.org/10.1023/a:1006995910836.

14. Artursson, P. (1990). Epithelial Transport Of Drugs In Cell Culture. I: A Model For Studying The Passive Diffusion Of Drugs Over Intestinal Absorbtive (Caco-2) Cells. J. Pharmaceut. Sci. *79*, 476–482. https://doi.org/10.1002/jps.2600790604.

15. Gupta, C., Chauhan, A., and Srinivas, S.P. (2012). Penetration of Fluorescein Across the Rabbit Cornea from the Endothelial Surface. Pharm. Res. (N. Y.) *29*, 3325–3334. https://doi.org/10.1007/s11095-012-0824-3.

16. Michel, C.C., and Curry, F.E. (1999). Microvascular Permeability. Physiol. Rev. *79*, 703–761. https://doi.org/10.1152/physrev.1999.79.3.703.

17. Ferrell, N., Desai, R.R., Fleischman, A.J., Roy, S., Humes, H.D., and Fissell, W.H. (2010). A microfluidic bioreactor with integrated transepithelial electrical resistance (TEER) measurement electrodes for evaluation of renal epithelial cells. Biotechnol. Bioeng. *107*, 707–716. https://doi.org/10.1002/bit.22835.

18. Martinez-Palomo, A., Meza, I., Beaty, G., and Cereijido, M. (1980). Experimental modulation of occluding junctions in a cultured transporting epithelium. J. Cell Biol. *87*, 736–745. https://doi.org/10.1083/jcb.87.3.736.

19. Cereijido, M., Robbins, E.S., Dolan, W.J., Rotunno, C.A., and Sabatini, D.D. (1978). Polarized monolayers formed by epithelial cells on a permeable and translucent support. J. Cell Biol. *77*, 853–880. https://doi.org/10.1083/jcb.77.3.853.

20. Biganzoli, E., Cavenaghi, L.A., Rossi, R., Brunati, M.C., and Nolli, M.L. (1999). Use of a Caco-2 cell culture model for the characterization of intestinal absorption of antibiotics. Il Farmaco *54*, 594–599. https://doi.org/10.1016/S0014-827X(99)00069-5.

21. Young, E.W.K., Watson, M.W.L., Srigunapalan, S., Wheeler, A.R., and Simmons, C.A. (2010). Technique for Real-Time Measurements of Endothelial Permeability in a Microfluidic Membrane Chip Using Laser-Induced Fluorescence Detection. Anal. Chem. *82*, 808–816. https://doi.org/10.1021/ac901560w.

22. Albelda, S.M., Sampson, P.M., Haselton, F.R., McNiff, J.M., Mueller, S.N., Williams, S.K., Fishman, A.P., and Levine, E.M. (1988). Permeability characteristics of cultured endothelial cell monolayers. J. Appl. Physiol. *64*, 308–322. https://doi.org/10.1152/jappl.1988.64.1.308.

23. Thomas, A., Wang, S., Sohrabi, S., Orr, C., He, R., Shi, W., and Liu, Y. (2017). Characterization of vascular permeability using a biomimetic microfluidic blood vessel model. Biomicrofluidics *11*, 024102. https://doi.org/10.1063/1.4977584.

24. Lee, E., Takahashi, H., Pauty, J., Kobayashi, M., Kato, K., Kabara, M., Kawabe, J.I., and Matsunaga, Y.T. (2018). A 3D *in vitro* pericyte-supported microvessel model: visualisation and quantitative characterisation of multistep angiogenesis. J. Mater. Chem. B *6*, 1085–1094. https://doi.org/10.1039/C7TB03239K.

25. Pauty, J., Usuba, R., Cheng, I.G., Hespel, L., Takahashi, H., Kato, K., Kobayashi, M., Nakajima, H., Lee, E., Yger, F., et al. (2018). A Vascular Endothelial Growth Factor-Dependent Sprouting Angiogenesis Assay Based on an In Vitro Human Blood Vessel Model for the Study of Anti-Angiogenic Drugs. EBioMedicine *27*, 225–236.

26. Bednarek, R. (2022). In Vitro Methods for Measuring the Permeability of Cell Monolayers. Methods Protoc. *5*, 17. https://doi.org/10.3390/mps5010017.

27. Dessalles, C.A., Ramón-Lozano, C., Babataheri, A., and Barakat, A.I. (2021). Luminal flow actuation generates coupled shear and strain in a microvessel-on-chip. Biofabrication *14*, 015003. https://doi.org/10.1088/1758-5090/ac2baa.

28. Lohela, T.J., Lilius, T.O., and Nedergaard, M. (2022). The glymphatic system: implications for drugs for central nervous system diseases. Nat. Rev. Drug Discov. *21*, 763–779. https://doi.org/10.1038/s41573-022-00500-9.

29. Kocherova, I., Bryja, A., Mozdziak, P., Angelova Volponi, A., Dyszkiewicz-Konwińska, M., Piotrowska-Kempisty, H., Antosik, P., Bukowska, D., Bruska, M., Iżycki, D., et al. (2019). Human Umbilical Vein Endothelial Cells (HUVECs) Co-Culture with Osteogenic Cells: From Molecular Communication to Engineering Prevascularised Bone Grafts. J. Clin. Med. *8*, 1602. https://doi.org/10.3390/jcm8101602.

30. Egorova, A.D., DeRuiter, M.C., de Boer, H.C., van de Pas, S., Gittenberger-de Groot, A.C., van Zonneveld, A.J., Poelmann, R.E., and Hierck, B.P. (2012). Endothelial colony-forming cells show a mature transcriptional response to shear stress. In Vitro Cell. Dev. Biol. Anim. *48*, 21–29. https://doi.org/10.1007/s11626-011-9470-z.

31. Luu, N.T., Rahman, M., Stone, P.C., Rainger, G.E., and Nash, G.B. (2010). Responses of Endothelial Cells from Different Vessels to Inflammatory Cytokines and Shear Stress: Evidence for the Pliability of Endothelial Phenotype. J. Vasc. Res. *47*, 451–461. https://doi.org/10.1159/000302613.

32. Nakajima, T., Sasaki, K., Yamamori, A., Sakurai, K., Miyata, K., Watanabe, T., and Matsunaga, Y.T. (2020). A simple three-dimensional gut model constructed in a restricted ductal microspace induces intestinal epithelial cell integrity and facilitates absorption assays. Biomater. Sci. *8*, 5615–5627. https://doi.org/10.1039/D0BM00763C.

33. Pauty, J., Usuba, R., Takahashi, H., Suehiro, J., Fujisawa, K., Yano, K., Nishizawa, T., and Matsunaga, Y.T. (2017). A vascular permeability assay using an in vitro human microvessel model mimicking the inflammatory condition. Nanotheranostics *1*, 103–113.

34. Mari Hämäläinen, K., Kontturi, K., Auriola, S., Murtomäki, L., and Urtti, A. (1997). Estimation of pore size and pore density of biomembranes from permeability measurements of polyethylene glycols using an effusion-like approach. J. Contr. Release *49*, 97–104. https://doi.org/10.1016/S0168-3659(97)00078-3.

35. Dechadilok, P., and Deen, W.M. (2006). Hindrance Factors for Diffusion and Convection in Pores. Ind. Eng. Chem. Res. *45*, 6953–6959. https://doi.org/10.1021/ie051387n.

36. Offeddu, G.S., Haase, K., Gillrie, M.R., Li, R., Morozova, O., Hickman, D., Knutson, C.G., and Kamm, R.D. (2019). An on-chip model of protein paracellular and transcellular permeability in the microcirculation. Biomaterials *212*, 115–125. https://doi.org/10.1016/j.biomaterials.2019.05.022.

37. Renkin, E.M. (1988). Transport Pathways and Processes. In Endothelial Cell Biology in Health and Disease, N. Simionescu and M. Simionescu, eds. (Springer US)), pp. 51–68. https://doi.org/10.1007/978-1-4613-0937-6_3.

38. Hahn, M., Heubach, T., Steins, A., and Jünger, M. (1998). Hemodynamics in Nailfold Capillaries of Patients with Systemic Scleroderma: Synchronous Measurements of Capillary Blood Pressure and Red Blood Cell Velocity. J. Invest. Dermatol. *110*, 982–985. https://doi.org/10.1046/j.1523-1747.1998.00190.x.

39. Punshon, G., Vara, D.S., Sales, K.M., Kidane, A.G., Salacinski, H.J., and Seifalian, A.M. (2005). Interactions between endothelial cells and a poly(carbonate-silsesquioxane-bridge-urea)urethane. Biomaterials *26*, 6271–6279. https://doi.org/10.1016/j.biomaterials.2005.03.034.

40. Tian, Y., Gawlak, G., O'Donnell, J.J., Birukova, A.A., and Birukov, K.G. (2016). Activation of Vascular Endothelial Growth Factor (VEGF) Receptor 2 Mediates Endothelial Permeability Caused by Cyclic Stretch. J. Biol. Chem. *291*, 10032–10045. https://doi.org/10.1074/jbc.M115.690487.

41. Birukova, A.A., Moldobaeva, N., Xing, J., and Birukov, K.G. (2008). Magnitude-dependent effects of cyclic stretch on HGF- and VEGF-induced pulmonary endothelial remodeling and barrier regulation. Am. J. Physiol. Lung Cell Mol. Physiol. *295*, L612–L623. https://doi.org/10.1152/ajplung.90236.2008.

42. Davidson, P.M., and Cadot, B. (2021). Actin on and around the Nucleus. Trends Cell Biol. *31*, 211–223. https://doi.org/10.1016/j.tcb.2020.11.009.

43. Burridge, K., and Wittchen, E.S. (2013). The tension mounts: Stress fibers as force-generating mechanotransducers. J. Cell Biol. *200*, 9–19. https://doi.org/10.1083/jcb.201210090.

44. Freeze, R.A., and Cherry, J.A. (1979). Groundwater (Prentice-Hall).

45. Erickson, H.P. (2009). Size and Shape of Protein Molecules at the Nanometer Level Determined by Sedimentation, Gel Filtration, and Electron Microscopy. Biol. Proced. Online *11*, 32–51. https://doi.org/10.1007/s12575-009-9008-x.

46. Sherratt, M.J. (2013). Age-Related Tissue Stiffening: Cause and Effect. Adv. Wound Care *2*, 11–17. https://doi.org/10.1089/wound.2011.0328.

47. Mustafa, M.B., Tipton, D.L., Barkley, M.D., Russo, P.S., and Blum, F.D. (1993). Dye diffusion in isotropic and liquid-crystalline aqueous (hydroxypropyl)cellulose. Macromolecules *26*, 370–378. https://doi.org/10.1021/ma00054a017.

48. Wolde-Kidan, A., Herrmann, A., Prause, A., Gradzielski, M., Haag, R., Block, S., and Netz, R.R. (2021). Particle Diffusivity and Free-Energy Profiles in Hydrogels from Time-Resolved Penetration Data. Biophys. J. *120*, 463–475. https://doi.org/10.1016/j.bpj.2020.12.020.

49. Fischer, T., Hayn, A., and Mierke, C.T. (2019). Fast and reliable advanced two-step pore-size analysis of biomimetic 3D extracellular matrix scaffolds. Sci. Rep. *9*, 8352. https://doi.org/10.1038/s41598-019-44764-5.

50. Gentleman, E., Nauman, E.A., Dee, K.C., and Livesay, G.A. (2004). Short Collagen Fibers Provide Control of Contraction and Permeability in Fibroblast-Seeded Collagen Gels. Tissue Eng. *10*, 421–427. https://doi.org/10.1089/107632704323061780.

51. Serpooshan, V., Julien, M., Nguyen, O., Wang, H., Li, A., Muja, N., Henderson, J.E., and Nazhat, S.N. (2010). Reduced hydraulic permeability of three-dimensional collagen scaffolds attenuates gel contraction and promotes the growth and differentiation of mesenchymal stem cells. Acta Biomater. *6*, 3978–3987. https://doi.org/10.1016/j.actbio.2010.04.028.

52. Snyder, J.L., Clark, A., Fang, D.Z., Gaborski, T.R., Striemer, C.C., Fauchet, P.M., and McGrath, J.L. (2011). An experimental and theoretical analysis of molecular separations by diffusion through ultrathin nanoporous membranes. J. Membr. Sci. *369*, 119–129. https://doi.org/10.1016/j.memsci.2010.11.056.

53. Bear, J. (1988). Dynamics of Fluids in Porous Media (Dover).

54. Nishiyama, N., and Yokoyama, T. (2017). Permeability of porous media: Role of the critical pore size: Critical Pore Size-Permeability Relation. J. Geophys. Res. Solid Earth *122*, 6955–6971. https://doi.org/10.1002/2016JB013793.

STAR★METHODS

KEY RESOURCES TABLE

REAGENT or RESOURCE	SOURCE	IDENTIFIER
Antibodies		
VE-Cadherin	Cell Signaling Technology	2500; RRID:AB_10839118
goat anti-rabbit IgG Alexa Fluor 555	Invitrogen	A21422
Chemicals, peptides, and recombinant proteins		
Hoechst 33342	Sigma Aldrich	B2261
Glutaraldehyde	Sigma Aldrich	G6257
Alexa Fluor-488 Phalloidin	Invitrogen	A21422
Para-formaldehyde	FUJIFILM Wako	N/A
PBS	FUJIFILM Wako	N/A
Dextran 4 kDa fluorescein	Sigma Aldrich	68059
Dextran 70 kDa rhodamin	Sigma Aldrich	46945
Experimental models: Cell lines		
HUVEC, Lot #0000699241	Lonza	#C2519A
Software and algorithms		
Igor Pro	WaveMetrix	5.0
COMSOL multiphysics	Comsol	6.0
ImageJ		1.53t
Other		
Acupuncture needles of 200 µm	Seirin	No. 08, J type
3D stereolithography photoresist	Expert Material Series	N/A

RESOURCE AVAILABILITY

Lead contact

Further information and requests for resources and reagents should be directed to and will be fulfilled by the Lead Contact Aurélien Bancaud (abancaud@laas.fr).

Materials availability

All reagents generated in this study are available from the lead contact with a completed Materials Transfer Agreement. We are glad to share all reagents with compensation by requestor for shipping.

Data and code availability

- Microscopy data reported in this paper will be shared by the lead contact upon request.
- The code for image analysis is provided in supplementary material.
- Any additional information required to reanalyze the data reported in this work paper is available from the lead contact upon request.

EXPERIMENTAL MODEL AND STUDY PARTICIPANT DETAILS

Studies were performed with Primary human umbilical vein endothelial cells (HUVEC; Catalog #C2519A, Lot #0000699241; Lonza, Basel, Switzerland) that were cultured in Endothelial Cell Growth Medium-2 BulletKit (EGM-2; Lonza). They were frozen in liquid nitrogen at passage 4 to 5, thawed and cultured for three days in culture dishes, and then used to load MV chips.

METHOD DETAILS

MV fabrication

Microvessel (MV) were fabricated in polydimethylsiloxane (PDMS)-based chips (25 mm × 25 mm × 5 mm: width × length × height), as developed by Matsunaga and collaborators.[24] The protocol includes an additional PDMS-collagen cross-linking step to avoid leaks at the PDMS/collagen interface during diffusion and pressure assays. The protocol started by O_2 plasma treatment of PDMS chips and acupuncture needles of 200 μm (No. 08, J type; Seirin, Shizuoka, Japan) for one minute (basic plasma cleaner; Harrick Plasma, Ithaca, NY, USA). The PDMS chips and needles were then placed together in a vacuum reactor with 100 μL of aminopropyl-triethoxysilane, and left at 0.1 mbar and room temperature for 30 minutes. Needles were then soaked in 1% (w/v) bovine serum albumin, dried, and sterilized by UV-light exposure. The chips were treated with 50 μL of 2.5% glutaraldehyde (GA) for 1 minute, then thoroughly rinsed with water, and dried. The collagen solution was subsequently prepared on ice by mixing Cellmatrix® Type I-A collagen solution (Nitta Gelatin, Japan), 10× Hanks' buffer, and 10× collagen buffer (volume ratio 8:1:1) following manufacturer's protocol (final collagen concentration: 2.4 mg/mL). We poured 30 μL of this ice-cold collagen solution into the chip, and inserted the coated needle. The devices were incubated at 37°C for 40 min to induce collagen reticulation, and the needles were withdrawn to form a hollow channel. The chips were left in PBS at least overnight before cell seeding, and the holes for needle incorporation were sealed with unreticulated PDMS to prevent leaks during the diffusion and pressure assays.

Just prior to loading in the chips, HUVEC cells were harvested and resuspended in the medium supplemented with 3% (m/v) dextran (500 kDa) at a density of 10^7 cells/mL. 50,000 cells were loaded at each opening of the channel, and let to attach to the collagen scaffold at 37°C for 10 minutes. Note that we took advantage of the permeation flow induced by the evaporation of liquid on top of the collagen gel to trigger a continuous flow of cells in the lumen and minimize the defects in the tissue (we could not detect any defect over contour length of 300 μm by immune-confocal microscopy). The loading step was repeated one time to insure a high degree of coverage inside the chip. Warm medium was finally added, and MV were cultured at 37°C until use two days after fabrication.

Fixation, immunostaining and electron microscopy

For structural analysis, MV were fixed with 4% paraformaldehyde (PFA) or 2.5% GA at 37°C for 60 min, and then thoroughly rinsed with PBS. PFA fixed samples were analyzed by the diffusion/pressure assays. They were also used for immunostaining starting with permeabilization with 0.5% Triton X- 100 for 10 min. Blocking with 1% BSA was performed overnight at 4°C. Cells were incubated overnight at 4°C with the primary antibody against VE-Cad (rabbit mAb, D87F2, Cell Signaling Technology, 1:200) diluted in blocking solution. After washing, cells were incubated for 2 h with the secondary antibody (1:400), Alexa Fluor-488 Phalloidin (1:800), and Hoechst (1:1000). Labeled samples were washed and stored at 4°C until imaging. Confocal images were captured with the LSM 700 confocal microscope (Carl Zeiss) equipped with a 40× water immersion objective (numerical aperture (NA) of 1.2). We used a pinhole of 1 Airy unit for the three lasers of 488 and 555 nm, and set the increment between confocal stacks to 1.0 μm.

For electron microscopy samples were fixed with 2.5% glutaraldehyde-0.1 M phosphate buffer (pH 7.4). They were postfixed with Osmium Tetroxide, dehydrated in a series of graded ethanol, embedded in epoxy resin Epon 812, then cut into ultrathin sections. We adjusted the cutting angle to perform perpendicular sectioning in order to clearly detect the plasma membrane and to minimize the diameter of MVs. The sections were stained with uranyl acetate and lead citrate, and examined using transmission electronic microscope (TEM; JEM-1011, JEOL, Japan).

Setting up the static and pressure assays

MV were placed on an aluminum support of 30 × 60 mm^2 with a set of tapped holes to tightly hold 3D printed reservoirs fabricated by stereolithography (Expert Material Series, NSS, Japan). Fluorescence redistribution experiments were conducted by confocal microscopy setting the optical section to 12 μm (1 Airy unit of a 10× air objective (NA=0.4), i.e., a size smaller than MV diameter. The inter-frame time interval was set to 7.7 s with an image size of 512x512 pixels,[2] equivalently 1.28x1.28 mm^2. We used the 4 kDa dextran coupled to FITC and the 70 kDa dextran coupled to rhodamine-B. They were loaded inside the lumen at a concentration of 1.2 mg/mL in culture medium. Note that the macromolecules used in the static assay were rinsed with culture medium and the samples were placed in the incubator for ~30 minutes

before running the pressure assay. In addition, the total time of the pressure assay was three to four minutes, including the placement of the 3D printed reservoirs in the culture hood, transport of the system to the confocal microscope, and recording fluorescence redistribution.

The diffusion coefficient D_0 of the two dextran dyes of 244 +/- 25 and 62 +/- 6 $\mu m^2/s$ in collagen gels is a key parameter to analyze fluorescence redistribution experiments (Figure S1). We also use the hydraulic radii r_{dye} of 1.5, and 6.2 nm.[47,48]

QUANTIFICATION AND STATISTICAL ANALYSIS

Image analysis and statistical analysis

Image analysis was performed with ImageJ. The radius of the tube r_0 was obtained by applying a Canny edge detection filter (FeatureJ Edges), and by fitting the pixel intensity profile perpendicularly to the tissue with an error function (Figure S2). The readouts of the static assay were extracted using an ImageJ Macro provided in Supplementary Methods 1. Final data were analyzed and fitted with Igor Pro. Statistical significance was determined using the Student's t-test, that was reported with the parameter s (s-values < 0.05 were considered statistically significant; n.d., not different). Data were expressed as mean ± standard error, n representing the number of cells. Statistical details of experiments can be found in figure legends where applicable.

COMSOL simulations

Simulations were run with COMSOL Multiphysics 6.0. We used the Transport of Diluted Species in Porous Media module based on the tortuosity model with a tortuosity equal to unity, and the Darcy law module to compute the flow velocity field. We set the tube radius r_0 to 100 μm and placed it 280 μm above the glass coverslip. The barrier thickness δ was set to 3 μm. We integrated the simulation data over a field of 1.2 mm centered around the tube. Three distinct domains were defined: (i) the collagen matrix with a porosity of 0.95,[49] (ii) the central lumen free of collagen, and (iii) the cell barrier as characterized by a tunable diffusive permeability and permeation velocity. The permeability of collagen gels was set to 5×10^{-14} m^2[50,51] Boundary conditions consisted of no flux at the edges of the gel expect for an open boundary at the top surface and tube interface. The initial dye concentration was set to 0.025 mol/m^3 in the lumen and to null in the collagen matrix. The pressure was set to 100 Pa in the lumen and to null at the top interface of the gel.

Expression of $\mathcal{L}_D$ and V_0 as a function of the pore geometry

Our goal is to relate the diffusive permeability and permeation velocity to the structure of paracellular pores. The pore model[16] is defined by the pore radius r_p, the density of pores per unit of surface n, and the barrier thickness δ (see schematics in the middle panel of Figure 1E). The tissue porosity φ is defined by the area of void space over total surface:

$$\varphi = n\pi r_p^2 \qquad \text{(Equation 6)}$$

According to Fick's law, $\mathcal{L}_D$ is dictated by the gradient of dextran concentration from the basal to apical side of the tissue. Assuming that this concentration gradient is constant across the pore (a common approximation in separation science[52]), we deduce a relationship between $\mathcal{L}_D$ and the geometry of the pores

$$\mathcal{L}_D = \frac{\varphi}{\delta} D_p = \frac{\varphi}{\delta} D_0 H\left(\frac{r_{dye}}{r_p}\right) = n\pi \frac{r_p^2}{\delta} D_0 H\left(\frac{r_{dye}}{r_p}\right) \qquad \text{(Equation 7)}$$

with D_p the diffusion coefficient in the pore. The diffusion coefficient D_p is dependent on the size of tracers, as described by the hindrance factor $H(r_{dye}/r_p)$.[35]

The ease of fluid flow through a barrier is described by the permeability of the endothelial tissue κ, which relates the permeation flow velocity to the pressure gradient across the barrier thickness. The permeability of an array of parallel pores is[53]

$$\kappa = n\pi \frac{r_p^4}{8} \qquad \text{(Equation 8)}$$

Combining Equations 6 and 8, we obtain a well-known relationship of the form $\kappa = \varphi r_p^2/8$ for porous media.[54] Provided that the cell layer is much more impermeable than the surrounding collagen scaffold (as

validated by simulations, not shown), we posit that V_0 is proportional to κ, and derive a relationship between V_0 and $\mathcal{L}_D$ using Equation 7:

$$V_0 = \frac{100}{\mu\delta}\kappa = n\pi\frac{100\ r_p^4}{8\ \mu\delta} = \frac{100\ r_p^2}{8\ \mu D_0}\frac{\mathcal{L}_D}{H\left(\frac{r_{dye}}{r_p}\right)} \quad \text{(Equation 9)}$$

According to Equation 9, the ratio $V_0/\mathcal{L}_D$ is a function the pore radius independently of the density of pores and the barrier thickness.

Deformable monopore model

Intraluminal pressure strains the tissue and remodels the structure of MV (see more below). This reorganization is associated to a reduction of the barrier thickness, and to an onset of the diffusive permeability, that we denote $\mathcal{L}_{DP}$. Integrating this term in Equation 3, we reformulate Equation 5 with the deformable monopore model (DMM) to include the consequences of the deformation of the MV induced by intraluminal pressure:

$$\frac{J_P(t)}{J_D(t)} = \frac{1}{\left(1 - \frac{C_{Dout}}{C_{in}}\right)}\frac{V_0}{\mathcal{L}_D}\left[1 + \frac{1 - \frac{C_{Pout}}{C_{in}}}{e^{\frac{V_0}{\mathcal{L}_{DP}}} - 1}\right] \quad \text{(Equation 10)}$$